Observation of Strong and Weak Thermalization in a Superconducting Quantum Processor

Fusheng Chen,[1,2,3,*] Zheng-Hang Sun,[4,5,*] Ming Gong,[1,2,3,*] Qingling Zhu,[1,2,3] Yu-Ran Zhang,[6] Yulin Wu,[1,2,3] Yangsen Ye,[1,2,3] Chen Zha,[1,2,3] Shaowei Li,[1,2,3] Shaojun Guo,[1,2,3] Haoran Qian,[1,2,3] He-Liang Huang,[1,2,3] Jiale Yu,[1,2,3] Hui Deng,[1,2,3] Hao Rong,[1,2,3] Jin Lin,[1,2,3] Yu Xu,[1,2,3] Lihua Sun,[1,2,3] Cheng Guo,[1,2,3] Na Li,[1,2,3] Futian Liang,[1,2,3] Cheng-Zhi Peng,[1,2,3] Heng Fan,[4,5,7,8,†] Xiaobo Zhu,[1,2,3,‡] and Jian-Wei Pan[1,2,3]

[1]*Hefei National Laboratory for Physical Sciences at Microscale and Department of Modern Physics, University of Science and Technology of China, Hefei, Anhui 230026, China*

[2]*Shanghai Branch, CAS Center for Excellence and Synergetic Innovation Center in Quantum Information and Quantum Physics, University of Science and Technology of China, Shanghai 201315, China*

[3]*Shanghai Research Center for Quantum Sciences, Shanghai 201315, China*

[4]*Institute of Physics, Chinese Academy of Sciences, Beijing 100190, China*

[5]*School of Physical Sciences, University of Chinese Academy of Sciences, Beijing 100190, China*

[6]*Theoretical Quantum Physics Laboratory, RIKEN Cluster for Pioneering Research, Wako-shi, Saitama 351-0198, Japan*

[7]*Songshan Lake Materials Laboratory, Dongguan 523808, Guangdong, China*

[8]*CAS Center for Excellent in Topological Quantum Computation, University of Chinese Academy of Sciences, Beijing 100190, China*

(Received 18 February 2021; accepted 16 June 2021; published 9 July 2021)

We experimentally study the ergodic dynamics of a 1D array of 12 superconducting qubits with a transverse field, and identify the regimes of strong and weak thermalization with different initial states. We observe convergence of the local observable to its thermal expectation value in the strong-thermalizaion regime. For weak thermalization, the dynamics of local observable exhibits an oscillation around the thermal value, which can only be attained by the time average. We also demonstrate that the entanglement entropy and concurrence can characterize the regimes of strong and weak thermalization. Our work provides an essential step toward a generic understanding of thermalization in quantum systems.

DOI: 10.1103/PhysRevLett.127.020602

Thermalization of an isolated quantum many-body system under nonequilibrium dynamics is a central topic in statistical mechanics [1–7]. For classical systems, statistical mechanics claims that with a longtime average, the Maxwell velocity distribution, independent of the initial condition, is satisfied [1]. In quantum cases, the choice of initial states plays an important role in the thermalization of closed nonintegrable many-body systems driven out of equilibrium. Numerical works [8,9] have shown that in a nonintegrable Ising model, when the effective inverse temperature of initial states is close to 0, the quenched states rapidly converge to their thermal expectations at a time after a short relaxation, and different from the classical counterpart, the time average is not necessary for achieving thermal equilibration. This phenomenon is regarded as strong (rapid) thermalization. In contrast, if the effective inverse temperature of initial states is sufficiently far away from 0, the temporal evolution of the local observable exhibits an obvious oscillation, with the longtime average attaining the thermal expectation value. Moreover, the decay of local observables and the growth of entanglement entropy (EE) are slow [10]. This phenomenon is known as weak (slow) thermalization. Recently, it has been numerically shown that regimes of strong and weak thermalization exist in the long-range Ising model describing trapped ions [10]. Nevertheless, a direct experimental comparison between strong thermalization and weak thermalization remains absent.

On the basis of the high-precision control, long coherence time, and the accurate readout, a superconducting quantum processor is an excellent platform for generating multipartite entangled states [11–13], characterizing quantum supremacy [14–16], and demonstrating variational quantum computation [17,18]. Moreover, by performing analog quantum simulations, the platform is also employed to study the phenomena in quantum many-body systems out of equilibrium, including quantum walks [19], many-body localization [20–22], dynamical phase transitions [23], and ergodic-localized junctions [24].

Here, a superconducting circuit, consisting of 12 transmon qubits, arranged in a 1D array with nearest-neighbor capacitive couplings, is employed to implement our experiments [see Fig. 1(a)]. The array of transmon qubits can be described by the 1D Bose-Hubbard model, where the anharmonicity of transmons is sufficiently large, preventing the doubly occupied state of transmons [19,25–27]. Thus, in the hard-core limit, the Bose-Hubbard model reduces to the integrable XX model [28–30]. To experimentally study

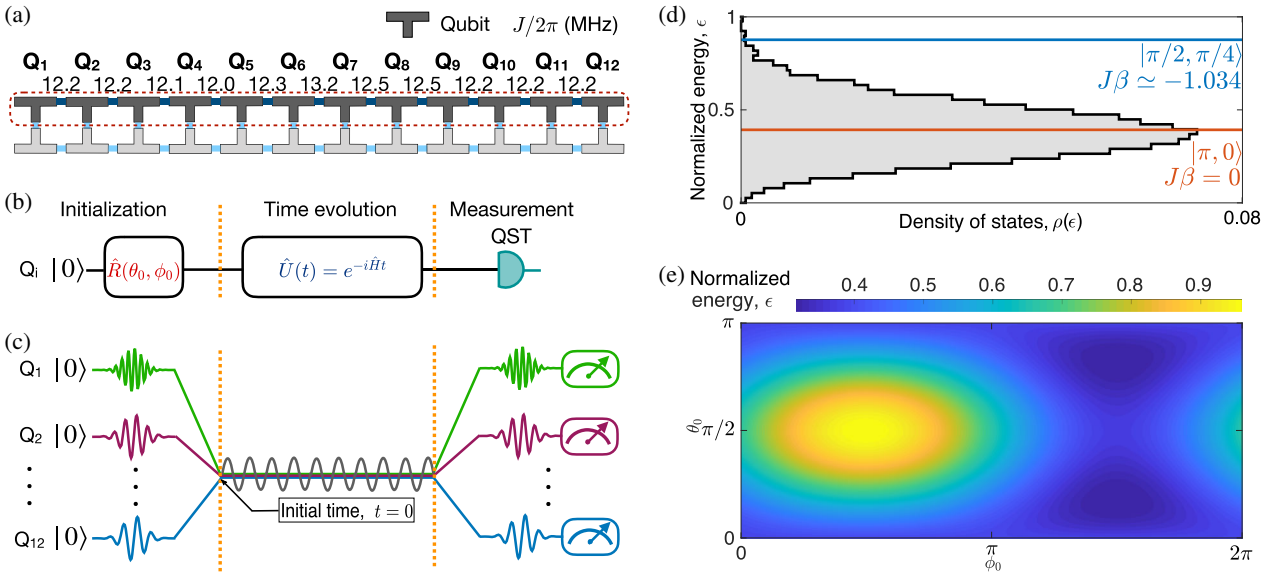

FIG. 1. (a) Architecture of the 24-qubit superconducting circuit. The qubits $Q_1 - Q_{12}$ are employed to realize a 1D nonintegrable model. (b) The schematic diagram of the pulse sequence used to observe strong and weak thermalization, which consists of three parts, i.e., initialization, evolution, and measurement. For the initialization, we prepare all qubits at $|\theta_0, \phi_0\rangle$, i.e., Eq. (2). Starting from the $|0\rangle$ state, all qubits are prepared at $|\theta_0, \phi_0'\rangle$ via the gate $\hat{R}(\theta_0, \phi_0')$ rotating $|0\rangle$ around the axis $\hat{n} = \cos(\phi_0')\hat{\sigma}^y - \sin(\phi_0')\hat{\sigma}^x$ by a angle θ_0. However, due to the dynamical phases accumulated in tunning qubits to the evolution point, ϕ_0' is not equal to ϕ_0. We calibrate the dynamical phases, and then correct all qubits to the same initial state $|\theta_0, \phi_0\rangle$. (c) The control waveforms corresponding to the pulse sequence in (b). The single-qubit pulses after $|0\rangle$ refer to the gate $\hat{R}(\theta_0, \phi_0)$. To realize the nonequilibrium quantum dynamics, the Z pulses and resonant microwave pulses (the sinusoidal line) are simultaneously applied to each qubit. After the evolution, quantum state tomography measurements are performed at idle points of the qubits and single-qubit pulses are required. (d) For the Hamiltonian (1), the density of states $\rho(\epsilon)$ as a function of the normalized energy ϵ obtained by the numerical simulation. The normalized energy of two initial states $|\pi, 0\rangle$ and $|\pi/2, \pi/4\rangle$ are highlighted. (e) The normalized energy of the initial state $|\theta_0, \phi_0\rangle$ as a function of θ_0 and ϕ_0.

strong and weak thermalization, we realize a nonintegrable system, using the superconducting qubit chain with a controllable transverse field. We observe the signatures of strong and weak thermalization via measuring the local observable with different initial states. Since the description of the local observable, using statistical mechanics, relies on the local entropy created by entanglement, the dynamics of the EE plays a key role in thermalization [31–35]. Thus, we study the EE of the single-qubit subsystems and show that the EE can distinguish the strong-thermalization regime from the weak one. Furthermore, we measure the concurrence [36] of the reduced density matrices of two nearest qubits, employing the tomographic readout, and observe thermal entanglement [37] in the presence of weak thermalization.

When we impose resonant microwave drives with a magnitude $g \simeq \lambda$ on all qubits, generating a local transverse field [23], the effective Hamiltonian of the superconducting circuit reads

$$\hat{H} = \lambda \sum_{j=1}^{11} (\hat{\sigma}_j^x \hat{\sigma}_{j+1}^x + \hat{\sigma}_j^y \hat{\sigma}_{j+1}^y) + g \sum_{j=1}^{12} \hat{\sigma}_j^y, \qquad (1)$$

where $\lambda = J/2$ with J being the nearest-neighbor coupling strength shown in Fig. 1(a). For details regarding the Hamiltonian (1), including its experimental realization and breakdown of integrability, as well as the performance of our device, see Supplemental Material [38].

To observe strong and weak thermalization, we initialize the system by preparing each qubit in the direction (θ_0, ϕ_0), which can be described as the spin coherent state

$$|\theta_0, \phi_0\rangle = \prod_{j=1}^{12} \left(\cos\frac{\theta_0}{2} |+Z\rangle_j + e^{-i\phi_0} \sin\frac{\theta_0}{2} |-Z\rangle_j \right), \qquad (2)$$

where $|+Z\rangle_j$ ($|-Z\rangle_j$) denotes the eigenstate of $\hat{\sigma}_j^z$ with the eigenvalue $+1$ (-1). Next, all qubits are biased to the working point to start the quench dynamics, $|\Psi_t\rangle = e^{-i\hat{H}t}|\theta_0, \phi_0\rangle$. We then tune the qubits to their idle points, and perform the quantum state tomography to reconstruct the one- and two-qubit density matrices. The experimental pulse sequence and control waveforms are shown in Figs. 1(b) and 1(c), respectively. There are three essential experimental requirements to be satisfied: (i) To realize the time evolution, all qubits should be tuned to the same frequency; (ii) The initial states of all qubits should be uniform at the start point of the time evolution; (iii) The local transverse fields of all qubits should be uniform during the evolution.

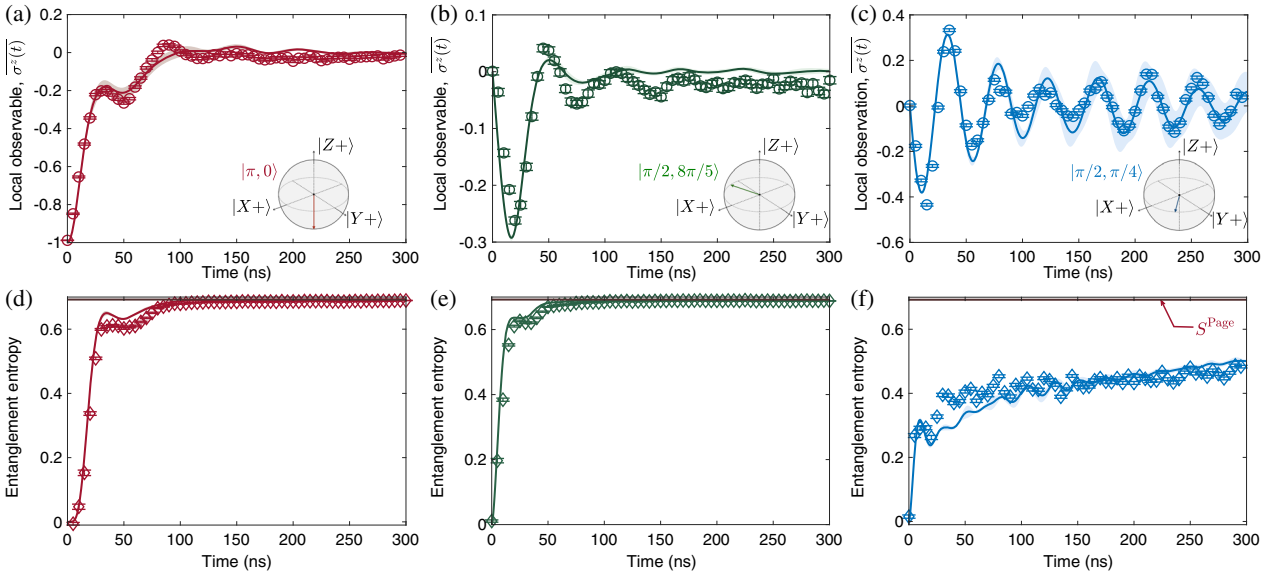

FIG. 2. (a) Experimental data of the time evolution of the local observable $\overline{\hat{\sigma}^z(t)}$ with the initial state $|\pi,0\rangle$. (b) As in (a), but for the initial state $|\pi/2,8\pi/5\rangle$. (c) As in (a), but for the initial state $|\pi/2,\pi/4\rangle$. (d) Experimental data of the time evolution of the entanglement entropy with the initial state $|\pi,0\rangle$. (e) As in (d), but for the initial state $|\pi/2,8\pi/5\rangle$. (f) As in (d), but for the initial state $|\pi/2,\pi/4\rangle$. The horizontal lines in (d)–(f) denote the Page value of the EE. The solid lines in (a)–(f) are numerical results without considering decoherence. The solid line in (f) is numerical results considering decoherence (see Supplemental Material [38] for the effects of decoherence). The shaded region shows the error bars of the numerical results, taking the uncertainties of the local field into consideration (see Supplemental Material [38]). The initial states are presented in Bloch spheres, where $|X+\rangle$, $|Y+\rangle$, and $|Z+\rangle$ are the eigenstate of σ^x, σ^y and σ^z with the eigenvalue $+1$, respectively.

These requirements are fulfilled with specific calibrations (see Supplemental Material for details [38]).

The occurrence of strong or weak thermalization relates closely to the effective inverse temperature β of $|\theta_0,\phi_0\rangle$, which can be obtained by solving $\mathrm{Tr}[\hat{H}(|\theta_0,\phi_0\rangle\langle\theta_0,\phi_0|-\hat{\rho}_\beta)]=0$, with $\hat{\rho}_\beta=e^{-\beta\hat{H}}/\mathrm{Tr}(e^{-\beta\hat{H}})$ being the thermal state [8]. Moreover, the quasiparticle explanation of weak thermalization indicates that initial states in the weak-thermalization regime are near the edge of the energy spectrum [9]. Here, we first consider two initial states $|\theta_0,\phi_0\rangle=|\pi/2,\pi/4\rangle$ and $|\pi,0\rangle$ whose effective inverse temperature is numerically estimated as $J\beta\simeq-1.034$ and 0, lying in the weak- and strong-thermalization regime, respectively. In addition to the effective inverse temperature, the regimes of strong and weak thermalization can be identified by defining the normalized energy of the initial state $|\theta_0,\phi_0\rangle$

$$\epsilon=\frac{\langle\theta_0,\phi_0|\hat{H}|\theta_0,\phi_0\rangle-E_{\mathrm{min}}}{E_{\mathrm{max}}-E_{\mathrm{min}}},\tag{3}$$

with E_{max} and E_{min} being the maximum and minimum eigenvalue of $\hat{H}$, respectively. In Fig. 1(d), the ϵ of the initial state $|\pi,0\rangle$ corresponds to the maximum density of states (DOS) $\rho(\epsilon)$, while the ϵ of the initial state $|\pi/2,\pi/4\rangle$ is close to the edge with $\rho(\epsilon)\simeq 0$. Moreover, in Fig. 1(e), we plot the normalized energy of different initial states $|\theta_0,\phi_0\rangle$, i.e., $\epsilon(\theta_0,\phi_0)$.

We start by characterizing strong and weak thermalization employing the local observable $\overline{\hat{\sigma}^z(t)}=1/12\sum_{j=1}^{12}\times\langle\Psi_t|\hat{\sigma}_j^z|\Psi_t\rangle$. Figures 2(a) and 2(c) present the experimental results of the time evolution of $\overline{\hat{\sigma}^z(t)}$ with initial states $|\pi,0\rangle$ and $|\pi/2,\pi/4\rangle$, respectively. It is shown that for the initial state $|\pi,0\rangle$ in the strong-thermalization regime, $\overline{\hat{\sigma}^z(t)}$ stably achieve the thermal value $\mathrm{Tr}(\hat{\rho}_\beta\hat{\sigma}_j^z)=0$ after $t\simeq 150$ ns. In contrast, for the initial state $|\pi/2,\pi/4\rangle$ in the weak-thermalization regime, $\overline{\hat{\sigma}^z(t)}$ strongly oscillates around the thermal value 0. It is noted that the anomalously persistent oscillation has also been observed in the Rydberg-atom quantum simulator [42]. This oscillation arises from the quantum many-body scars, that is a mechanism different from weak thermalization [43]. In addition, we measure the dynamics of $\overline{\hat{\sigma}^z(t)}$ with the initial state $|\pi/2,8\pi/5\rangle$, which also lies in the strong-thermalization regime, since its effective inverse temperature is $J\beta\simeq 0$. The results, depicted in Fig. 2(b), show that even the behavior of short relaxation is different from that with the initial state $|\pi,0\rangle$, the local observable also has a stationary value near the thermal value 0 after $t\simeq 150$ ns, which is a hallmark of strong thermalization.

Next, we consider the von Neumann EE, $S=-\mathrm{Tr}[\hat{\rho}_j\ln(\hat{\rho}_j)]$, where $\hat{\rho}_j$ is the reduced density matrix of the jth qubit. We average the EE over all qubit sites.

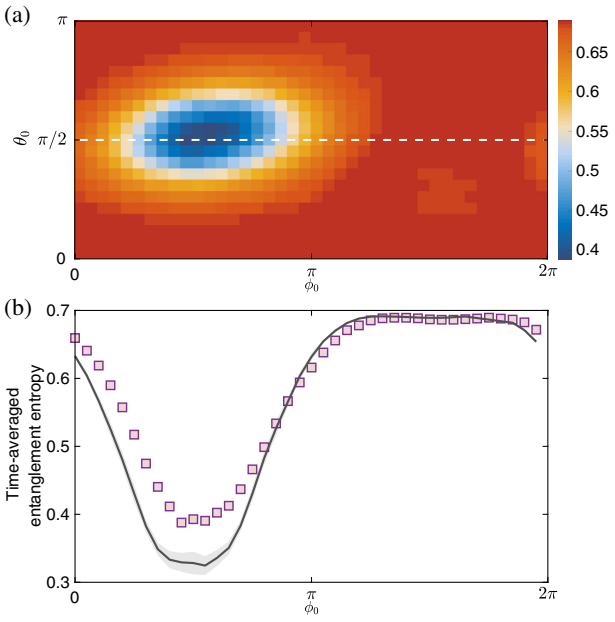

FIG. 3. (a) Experimental data of the time-averaged EE with initial states $|\theta_0, \phi_0\rangle$ plotted in the $\phi_0 - \theta_0$ plane. (b) Experimental data of the time-averaged EE with initial states $|\pi/2, \phi_0\rangle$. The white dashed line in (a) highlights $\theta_0 = \pi/2$. The solid line in (b) shows the numerical result considering decoherence (see Supplemental Material [38] for the effects of decoherence). The shaded region shows the error bars of the numerical results, taking the uncertainties of the local field into consideration (see Supplemental Material [38]).

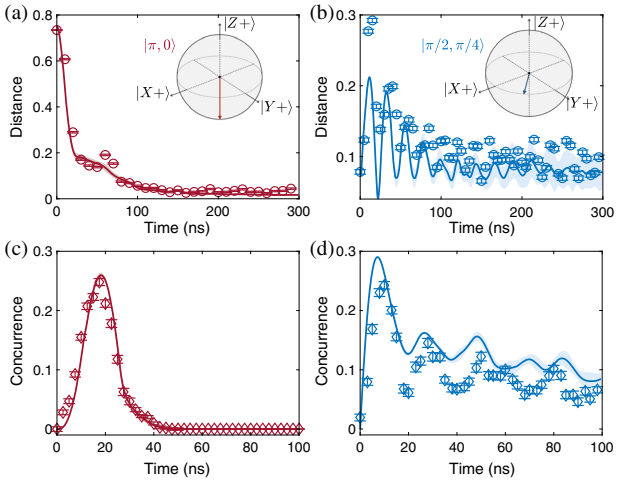

FIG. 4. (a) Experimental data of the trace distance between the nonequilibrium and thermal states with the initial state $|\pi, 0\rangle$. (b) As in (a), but for the initial state $|\pi/2, \pi/4\rangle$. (c) Experimental data of the concurrence with the initial state $|\pi, 0\rangle$. (d) As in (c), but for the initial state $|\pi/2, \pi/4\rangle$. The solid lines in (a) and (c) are numerical results without considering decoherence. The solid lines in (b) and (c) are numerical results considering decoherence (see Supplemental Material [38] for the effects of decoherence). The shaded region shows the error bars of the numerical results, taking the uncertainties of the local field into consideration (see Supplemental Material [38]). The initial states are presented in Bloch spheres, where $|X+\rangle$, $|Y+\rangle$, and $|Z+\rangle$ are the eigenstate of σ^x, σ^y and σ^z with the eigenvalue $+1$, respectively.

The dynamics of the EE, with the initial states $|\pi, 0\rangle$ and $|\pi/2, 8\pi/5\rangle$ in the regime of strong thermalization, are displayed in Figs. 2(d) and 2(e), respectively. We observe that for strong thermalization, the EE rapidly reaches the Page value $S^{\text{Page}} \simeq 0.692$ as the maximum EE of a single-qubit subsystem of a total system in the random pure state [44]. However, for weak thermalization, the nonequilibrium dynamics gains the EE smaller than the Page value [Fig. 2(f)].

Furthermore, we study the time-averaged EE between 100 and 200 ns with different initial states $|\theta_0, \phi_0\rangle$. In Fig. 3(a), we show the experimental data of time-averaged EE with different initial states $|\theta_0, \phi_0\rangle$, which bears a close resemblance to the normalized energy in Fig. 1(e). Specifically, with $\theta_0 = \pi/2$, around $\phi_0 \simeq 3\pi/2$, $\epsilon \simeq 0.4$, and the DOS $\rho(\epsilon)$ becomes the maximum [see Figs. 1(d) and 1(e)]. Thus, it can be predicted that strong thermalization occurs in this regime. Additionally, according to the results in Figs. 1(d) and 1(e), the normalized energy is near 1 at $\phi_0 = \pi/2$, where the DOS is close to 0, and the degree of thermalization is the weakest. The experimental data of the time-averaged EE, with $\theta_0 = \pi/2$ and different ϕ_0, are presented in Fig. 3(b). There is a minimum of the EE around $\phi_0 = \pi/2$, corresponding to the weakest thermalization. Moreover, the maximum EE reveals a regime of strong thermalization with $\theta_0 = \pi/2$ and $\phi_0 \in [1.3\pi, 1.9\pi]$.

The trace distance between the nonequilibrium state $\hat{\rho}_t = |\Psi_t\rangle\langle\Psi_t|$ and the thermal state $\hat{\rho}_\beta$, with the β being the effective inverse temperature of the initial state, i.e., $\frac{1}{2}\text{Tr}(|\hat{\rho}_t - \hat{\rho}_\beta|)$, can diagnose quantum thermalization [31]. It has been numerically shown that the distance monotonically decays to 0 for strong thermalization. With initial states in the weak-thermalization regime, the decay of the distance can also be observed but with a strong fluctuation [8].

We measure the reduced density matrix $\hat{\rho}_t^{j,j+1}$ of the subsystem consisting of the jth and $(j+1)$th qubit, using the quantum state tomography. For the initial state $|\pi, 0\rangle$, the effective inverse temperature is $J\beta = 0$, and the corresponding two-qubit thermal state is $\hat{I}/4$ with $\hat{I}$ being an identity matrix. Then, the trace distance between $\hat{\rho}_t^{j,j+1}$ and $\hat{I}/4$, averaged over the qubit site j, can be directly obtained. Similarly, by considering the thermal states $\hat{\rho}_\beta^{j,j+1}$ with $J\beta \simeq -1.034$, the dynamics of the trace distance, with the initial state $|\pi/2, \pi/4\rangle$, can also be measured. As shown in Figs. 4(a) and 4(b), the trace distance decays during the time evolution for both strong and weak thermalization, indicating the tendency $\hat{\rho}_t^{j,j+1} \simeq \hat{\rho}_\beta^{j,j+1}$. However, for weak thermalization, the trace distance strongly oscillates [Fig. 4(b)].

Finally, we experimentally investigate the concurrence of the two-qubit reduced density matrix $\hat{\rho}_t^{j,j+1}$, which is

defined as $E(\hat{\rho}) = \max\{0, \sqrt{\gamma_1} - \sqrt{\gamma_2} - \sqrt{\gamma_3} - \sqrt{\gamma_4}\}$, where $\gamma_1, \ldots, \gamma_4$ are eigenvalues listed in decreasing order of the matrix $\Gamma = \hat{\rho}(\hat{\sigma}^y \otimes \hat{\sigma}^y)\hat{\rho}^*(\hat{\sigma}^y \otimes \hat{\sigma}^y)$ [36]. The time evolution of the concurrence, with the initial state $|\pi, 0\rangle$ and $|\pi/2, \pi/4\rangle$, is presented in Figs. 4(c) and 4(d), respectively. We observe that the concurrence vanishes after $t \simeq 50$ ns for strong thermalization. Whereas, the concurrence preserves a finite value with the initial state in the weak-thermalization regime, which can be interpreted as the thermal entanglement, i.e., the concurrence in thermal states $\hat{\rho}_\beta$ [37], according to $\hat{\rho}_t^{j,j+1} \simeq \hat{\rho}_\beta^{j,j+1}$ as a result of the ergodic dynamics in the weak-thermalization regime. The numerics of the concurrence in thermal states $\hat{\rho}_\beta$ with different β are presented in Supplemental Material [38].

In summary, we have provided clear experimental evidence for characterizing the regimes of strong and weak thermalization. Weak thermalization, with a slow growth of the EE, has the potential for generating states with long-lived coherence and stabilizing the phases of matter far away from equilibrium, such as Floquet symmetry-protected topological phases [45], discrete time crystals [46], many-body localized phase [6,47,48], and dynamical paramagnetic and ferromagnetic phases [23,49]. Our work also indicates that the 1D array of superconducting qubits can be a promising platform for exploring the issues at the foundation of quantum thermodynamics.

The authors thank the USTC Center for Micro- and Nanoscale Research and Fabrication. The authors also thank QuantumCTek Co., Ltd. for supporting the fabrication and the maintenance of room temperature electronics. This research was supported by the National Key R&D Program of China (Grants No. 2017YFA0304300, No. 2018YFA0306703, No. 2016YFA0302104, No. 2016YFA0300600), the Chinese Academy of Sciences, and Shanghai Municipal Science and Technology Major Project (Grant No. 2019SHZDZX01), the Strategic Priority Research Program of Chinese Academy of Sciences (Grant No. XDB28000000), Japan Society for the Promotion of Science (JSPS) Postdoctoral Fellowship (Grant No. P19326), JSPS KAKENHI (Grant No. JP19F19326), the National Natural Science Foundation of China (Grants No. 11574380, No. 11905217, No. 11934018, No. 11774406), the Key-Area Research and Development Program of Guangdong Province (Grant No. 2020B0303030001), and Anhui Initiative in Quantum Information Technologies.

*These authors contributed equally to this work.
†hfan@iphy.ac.cn
‡xbzhu16@ustc.edu.cn

[1] G. Gallavotti, *Statistical Mechanics: A Short Treatise* (Springer, Berlin, 1999).
[2] J. M. Deutsch, Phys. Rev. A **43**, 2046 (1991).
[3] M. Srednicki, Phys. Rev. E **50**, 888 (1994).
[4] M. Rigol, V. Dunjko, and M. Olshanii, Nature (London) **452**, 854 (2008).
[5] A. Polkovnikov, K. Sengupta, A. Silva, and M. Vengalattore, Rev. Mod. Phys. **83**, 863 (2011).
[6] R. Nandkishore and D. A. Huse, Annu. Rev. Condens. Matter Phys. **6**, 15 (2015).
[7] J. Eisert, M. Friesdorf, and C. Gogolin, Nat. Phys. **11**, 124 (2015).
[8] M. C. Bañuls, J. I. Cirac, and M. B. Hastings, Phys. Rev. Lett. **106**, 050405 (2011).
[9] C.-J. Lin and O. I. Motrunich, Phys. Rev. A **95**, 023621 (2017).
[10] F. Liu, R. Lundgren, P. Titum, G. Pagano, J. Zhang, C. Monroe, and A. V. Gorshkov, Phys. Rev. Lett. **122**, 150601 (2019).
[11] M. Gong, M.-C. Chen, Y. Zheng, S. Wang, C. Zha, H. Deng *et al.*, Phys. Rev. Lett. **122**, 110501 (2019).
[12] C. Song, K. Xu, H. Li, Y.-R. Zhang, X. Zhang, W. Liu *et al.*, Science **365**, 574 (2019).
[13] K. X. Wei, I. Lauer, S. Srinivasan, N. Sundaresan, D. T. McClure, D. Toyli, D. C. McKay, J. M. Gambetta, and S. Sheldon, Phys. Rev. A **101**, 032343 (2020).
[14] F. Arute, K. Arya, R. Babbush, D. Bacon, J. C. Bardin, R. Barends *et al.*, Nature (London) **574**, 505 (2019).
[15] S. Boixo, S. V. Isakov, V. N. Smelyanskiy, R. Babbush, N. Ding, Z. Jiang, M. J. Bremner, J. M. Martinis, and H. Neven, Nat. Phys. **14**, 595 (2018).
[16] C. Neill, P. Roushan, K. Kechedzhi, S. Boixo, S. V. Isakov, V. Smelyanskiy *et al.*, Science **360**, 195 (2018).
[17] F. Arute, K. Arya, R. Babbush, D. Bacon, J. C. Bardin, R. Barends *et al.*, Science **369**, 1084 (2020).
[18] M.-C. Chen, M. Gong, X. Xu, X. Yuan, J.-W. Wang, C. Wang *et al.*, Phys. Rev. Lett. **125**, 180501 (2020).
[19] Z. Yan, Y.-R. Zhang, M. Gong, Y. Wu, Y. Zheng, S. Li *et al.*, Science **364**, 753 (2019).
[20] Q. Guo, C. Cheng, Z.-H. Sun, Z. Song, H. Li, Z. Wang *et al.*, Nat. Phys. **17**, 234 (2021).
[21] K. Xu, J.-J. Chen, Y. Zeng, Y.-R. Zhang, C. Song, W. Liu *et al.*, Phys. Rev. Lett. **120**, 050507 (2018).
[22] B. Chiaro, C. Neill, A. Bohrdt, M. Filippone, F. Arute, K. Arya *et al.*, arXiv:1910.06024.
[23] K. Xu, Z.-H. Sun, W. Liu, Y.-R. Zhang, H. Li, H. Dong *et al.*, Sci. Adv. **6**, eaba4935 (2020).
[24] C. Zha, V. M. Bastidas, M. Gong, Y. Wu, H. Rong, R. Yang *et al.*, Phys. Rev. Lett. **125**, 170503 (2020).
[25] Q. Zhu, Z.-H. Sun, M. Gong, F. Chen, Y.-R. Zhang, Y. Wu *et al.*, arXiv:2101.08031.
[26] P. Roushan, C. Neill, J. Tangpanitanon, V. M. Bastidas, A. Megrant, R. Barends *et al.*, Science **358**, 1175 (2017).
[27] J. Koch, T. M. Yu, J. Gambetta, A. A. Houck, D. I. Schuster, J. Majer *et al.*, Phys. Rev. A **76**, 042319 (2007).
[28] M. A. Cazalilla, R. Citro, T. Giamarchi, E. Orignac, and M. Rigol, Rev. Mod. Phys. **83**, 1405 (2011).
[29] M. Cramer, A. Flesch, I. P. McCulloch, U. Schollwöck, and J. Eisert, Phys. Rev. Lett. **101**, 063001 (2008).
[30] E. Lieb, T. Schultz, and D. Mattis, Ann. Phys. (N.Y.) **16**, 407 (1961).
[31] A. M. Kaufman, M. E. Tai, A. Lukin, M. Rispoli, R. Schittko, P. M. Preiss, and M. Greiner, Science **353**, 794 (2016).

[32] C. Neill, P. Roushan, M. Fang, Y. Chen, M. Kolodrubetz, Z. Chen *et al.*, Nat. Phys. **12**, 1037 (2016).
[33] Y. O. Nakagawa, M. Watanabe, H. Fujita, and S. Sugiura, Nat. Commun. **9**, 1635 (2018).
[34] H. Kim and D. A. Huse, Phys. Rev. Lett. **111**, 127205 (2013).
[35] S. Popescu, A. Short, and A. Winter, Nat. Phys. **2**, 754 (2006).
[36] W. K. Wootters, Phys. Rev. Lett. **80**, 2245 (1998).
[37] M. C. Arnesen, S. Bose, and V. Vedral, Phys. Rev. Lett. **87**, 017901 (2001).
[38] See Supplemental Material at http://link.aps.org/supplemental/10.1103/PhysRevLett.127.020602 for details about the device information and the system Hamiltonian, the calibration of initial states and the transverse field, the crosstalk effect, the impact of decoherence, and additional numerics of the concurrence, which includes Refs. [39–41].
[39] Y. Y. Atas, E. Bogomolny, O. Giraud, and G. Roux, Phys. Rev. Lett. **110**, 084101 (2013).
[40] J. R. Johansson, P. D. Nation, and F. Nori, Comput. Phys. Commun. **183**, 1760 (2012).
[41] J. R. Johansson and P. D. Nation, and F. Nori, Comput. Phys. Commun. **184**, 1234 (2013).
[42] H. Bernien, S. Schwartz, A. Keesling, H. Levine, A. Omran, H. Pichler *et al.*, Nature (London) **551**, 579 (2017).
[43] C. Turner, A. A. Michailidis, D. A. Abanin, M. Serbyn, and Z. Papić, Nat. Phys. **14**, 745 (2018).
[44] D. N. Page, Phys. Rev. Lett. **71**, 1291 (1993).
[45] A. C. Potter, T. Morimoto, and A. Vishwanath, Phys. Rev. X **6**, 041001 (2016).
[46] D. V. Else, C. Monroe, C. Nayak, and N. Y. Yao, Annu. Rev. Condens. Matter Phys. **11**, 467 (2020).
[47] E. Altman, Nat. Phys. **14**, 979 (2018).
[48] D. A. Abanin, E. Altman, I. Bloch, and M. Serbyn, Rev. Mod. Phys. **91**, 021001 (2019).
[49] J. Zhang, G. Pagano, P. W. Hess, A. Kyprianidis, P. Becker, H. Kaplan, A. V. Gorshkov, Z.-X. Gong, and C. Monroe, Nature (London) **551**, 601 (2017).